Research paper

Boron-10 stimulated helium production and accelerated radiation displacements for rapid development of fusion structural materials

Yunsong Jung [a, b], Ju Li [a, *]

[a] Department of Nuclear Science and Engineering and Department of Materials Science and Engineering, Massachusetts Institute of Technology, Cambridge, MA, 02139, USA
[b] Korea Institute of Fusion Energy, Daejeon, 34133, Republic of Korea

ARTICLE INFO

ABSTRACT

Boron doping, combined with neutron capture in fission reactors, has been used to simulate the helium effect on fusion structural materials. However, inhomogeneous helium bubble formation was often observed due to boron segregation to grain boundaries. The excess radiation displacements due to $^{10}B(n, \alpha)^7Li$ reaction, the high-energy lithium and helium ions, also were not accounted for, which can significantly accelerate the displacements-per-atom (dpa) accumulation alongside helium production (appm). Hereby an isotopically pure ^{10}B doping approach is proposed to simulate the extreme environment inside fusion reactors with a high He appm-to-dpa ratio of about 10, which is about $10^2 \times$ larger than in fission reactors. Computational modeling showed that ~13% of total radiation displacement was induced by $^{10}B(n, \alpha)^7 Li$ in the case of 1 000 appm ^{10}B doped Fe samples, which becomes even greater with increasing ^{10}B loading. Spatially homogenous radiation damage and helium generation are predicted for grain sizes less than 1 μm, even if the boron partially formed precipitates or segregates on grain boundaries. Feasibility studies with various ^{10}B doping (and ^{235}U-codoping) levels in research reactors showed the estimated helium generation and radiation damage would significantly mimic fusion conditions and greatly expedite fusion materials testing, from many years down to months.

© 2023 Published by Elsevier B.V. on behalf of The Chinese Ceramic Society. This is an open access article under the CC BY-NC-ND license (http://creativecommons.org/licenses/by-nc-nd/4.0/).

1. Introduction

Harnessing fusion power is the holy grail of energy science and engineering and may be the key to space explorations and climate adaptation. Deuterium-tritium fusion in a burning plasma, the most promising route, produces 3.5 MeV helium ions and 14.1 MeV neutrons. Neutrons are much more deeply penetrating in materials than ions and electrons, which is both a blessing and a curse. On one hand, this allows (a) energy transfer to a coolant and (b) breeding of tritium, that happen many centimeters away from the burning plasma, separated by a solid vacuum vessel [1], the equivalent of the nuclear fuel cladding in fission reactor core. On the other hand, the fast neutrons streaming through such vacuum vessel (VV) would cause not only massive displacement damages (measured by displacements per atom, dpa), but also numerous helium atoms (measured by atomic parts-per-million, appm)

produced inside the material by unavoidable (n, α) transmutation reactions, whose cross-section in Fe is ~40 mb for 14.1 MeV neutron. Fusion structural materials must therefore endure both high-energy neutrons and gas-atom generation and implantation, which can cause severe degradation of their structural integrity. The internalized He causes embrittlement and swelling of fusion materials [2,3], and is considered the more component-life-limiting factor than dpa [4], at the high operating temperatures of interest to fusion [5]. In other words, while both dpa and appm (He) contribute to damaging the vacuum vessel, in the temperature range for running the fusion reactor VV economically which is $\geq$ 600 °C, appm (He) is the more severe threat. This is opposite from the situation in fission research reactors and commercial fission power reactors, where the neutron spectrum is much softer, and the appm (He)-to-dpa ratio is about 0.1, and Helium plays only a secondary role in the damage compared to dpa. In contrast, in fusion reactors the appm-to-dpa ratios in Fe and W were estimated to be ~10 and ~0.5 [6], respectively, and thus the helium damage is much more prominent (although the dpa effect cannot be neglected).

To advance controllable fusion energy, we need to design and

qualify novel structural materials that can survive thousands of appm (He) [7] and hundreds of dpa of radiation displacements, in order to ensure a few years of full-power operations—the minimum for economic fusion power generation. However, the lack of high-flux fast neutrons for materials testing leads to a chicken-and-egg problem. On one hand, we do not yet have full confidence that any materials available today can survive thousands of appm (He) with hundreds of dpa at $\geq 600°C$ in contact with corrosive coolants. On the other hand, the lack of such materials also impedes the establishment and safe operation of such sources. As background, fast-neutron sources are difficult to come by. At present, Russia operates BN-600 and BN-800 fast neutron reactors, China operates China Experimental Fast Reactor (CEFR), all liquid sodium cooled, but there is no fast neutron fission reactor operating in Europe and the Americas. Currently, there is no facility anywhere in the world that can provide a neutron energy spectrum and fluence close to economic fusion power reactor conditions. The test facility for fusion neutron sources, such as the proposed International Fusion Materials-Irradiation Facility (IFMIF) and Advanced Fusion Neutron Source (A-FNS) are not expected to be available for more than 10 years. To simulate the 14.1 MeV-neutron effects on fusion reactor materials, experimental techniques such as multi-ion beam irradiation [8,9], spallation neutron sources [10,11], boron doping [12–19], and nickel doping [20–22] have been proposed.

The boron doping approach has been used to accelerate helium production by boron-neutron capture $^{10}B(n, \alpha)^7Li$ reaction using softer-spectrum neutrons, which are much more broadly available at fission reactors around the world, for example, the MIT Nuclear Research Reactor (MITR), the High Flux Isotope Reactor (HFIR) at Oak Ridge National Laboratory, and commercial fission power reactors. ^{10}B has an exceptionally high thermal neutron capture cross-section of 3,840 b, thus ^{10}B produces helium $10^5 \times$ faster under thermal neutrons than Fe under fast neutrons. Chemically pre-doping of material under investigation by ^{10}B can greatly boost internal helium production, with the potential to mimic fusion-spectrum exposure of multiple years in a matter of weeks (see computational predictions below), in the sense of reaching the same levels of appm (He) and dpa simultaneously. However, the problems of borides and boron segregation to grain boundaries (GB) need to be considered. GB segregation of boron was observed in 316 stainless steel doped with 0.5%(in mass) boron, even though rapid quenching was employed in attempting to create a homogeneous boron distribution [18]. Boron-containing precipitates such as B(C,N), and $(Fe,Cr)_2B$ were also often found in boron-containing alloys [23,24]. ^{10}B-doped EUROFER97, one of the reduced activation ferritic martensitic steels, was neutron-irradiated up to 16 dpa and showed a high density of He bubbles around BN precipitates [18]. Also, after reviewing the literature we found that the radiation displacements induced by high energy Li (~0.8 MeV) and He (~1.5 MeV) ions emitted from $^{10}B(n, \alpha)^7Li$ reactions were not modeled and generally ignored [15,25], leading to errors in the dpa estimation.

In this study, we computationally designed a methodology to mimic fusion-spectrum exposure of material using soft-spectrum neutron capture with ^{10}B-doped materials. The boron solubility and solubility enhancement in iron and tungsten were discussed to suppress the boron segregation. The radiation damage induced by Li and He ions emitted from $^{10}B(n, \alpha)^7Li$ reactions was calculated. Feasibility studies were conducted for various ^{10}B concentrations. The flow chart of the advanced ^{10}B doping methodology was designed from fabrication to post-irradiation examination. We will show that the right He appm-to-dpa ratio of ~10, appropriate for fusion conditions, can be achieved by such a surrogate test. Furthermore, the surrogate test can be much faster due to the huge thermal neutron capture cross-section of 3,840 b of ^{10}B (in contrast,

^{11}B has a negligible thermal neutron capture cross-section of 0.005 b). ^{10}B and ^{11}B has natural abundance of 19.8% and 80.2%, respectively, thus using enriched ^{10}B, which is commercially available, would give $5 \times$ speedup and dose rate. This way, we can shorten the radiation campaign to much less than a year, while still reaching thousands of appm (He) and hundreds of dpa, thus allowing greatly accelerated fusion structural materials selection and optimization.

2. Methods

Radiation damage and helium concentrations induced by $^{10}B(n, \alpha)^7Li$ reactions in pure iron were estimated based on computer simulations using the Stopping and Range of Ions in Matter (SRIM-2013) code with the full cascades damage energy method, which provides the highest accuracy for vacancy production [26,27]. The vacancy production was calculated using the damage energy method given in Eqn. (1) with recommended displacement threshold energy (40 eV for Fe and 90 eV for W) and lattice binding energy (5.8 eV for Fe and 13.2 eV for W) [27,28].

$$\nu_{NRT} = 0.8 T_{dam}/2E_d$$
$$T_{dam} = E_{recoil} - E_{ioniz} \tag{1}$$

where ν_{NRT} is the Norgett, Robinson, and Torrens (NRT) displacements, T_{dam} is the damage energy, E_d is the displacement threshold energy, E_{recoil} is the energy absorbed by recoils, and E_{ioniz} is the ionization energy loss of the recoil ions.

3. Results and discussion

3.1. Radiation damage and helium distribution induced by $^{10}B(n, \alpha)^7Li$ reactions

The usage of $^{10}B(n, \alpha)^7Li$ reactions can accelerate not only helium production but also radiation damage induced by highly energetic Li and He product nuclei, as shown in Fig. 1. Unlike nickel doping which produces long-lived radio-isotopes, no long-lived radioactive elements are produced from boron transmutation, which makes it relatively easy to handle after the neutron irradiation (One does need to consider the effect of thermal neutron transmutation on the base material, for example, $^{13}C(n, \gamma)^{14}C$, as the natural abundance of carbon-13 is ~1% and carbon-14 has a half-life of 5,730 years). There are two types of $^{10}B(n, \alpha)^7Li$ reactions that emit MeV-scale Li and He ions as given in Eqn. (2). An additional
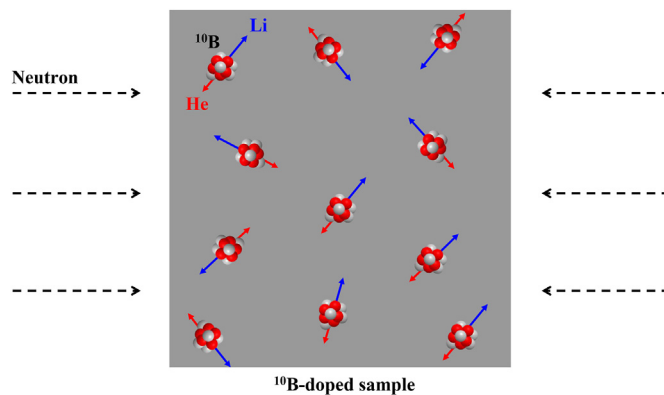

Fig. 1. Schematic illustration of ^{10}B doping methodology to simulate helium production and dpa accumulation (Not to scale). Note that the outgoing Li (blue) and He (red) ions have spherically random momenta, unlike the energetic ions produced by ion accelerators, thus mitigating potential polarization artifacts [29].

benefit of the dpa generation by Eqn. (2) is that the radiation damages are isotropic, unlike that created with accelerator-driven ion beam where the high momentum monodispersity can create polarization artifacts and vacancy-interstitial imbalances in the typical 1D geometry [29].

as r^{-2} due to finite $\rho(x = 0)$ shown in Figs. 2 and 3, and the other peak will occur at $r_{peak}>0$ but with $r_{peak} < x_{peak}\equiv$argmax $\rho(x)$. That is, the peak damage and helium concentration will occur closer to the boride particle than the standard "Bragg peak" in 1D geometry. This effect is illustrated in Fig. 4.

$$
\begin{aligned}
{}^{10}_{5}\text{B} + {}^{1}_{0}\text{n}_{\text{thermal}} \quad &\rightarrow (94\%)\ {}^{7}_{3}\text{Li}^{3+}(0.840\ \text{MeV}) + {}^{4}_{2}\text{He}^{2+}(1.470\ \text{MeV}) + \gamma\ (0.48\ \text{MeV}) \\
&\rightarrow (6\%)\ {}^{7}_{3}\text{Li}^{3+}(1.015\ \text{MeV}) + {}^{4}_{2}\text{He}^{2+}(1.777\ \text{MeV})
\end{aligned}
\tag{2}
$$

The depth-dependent vacancy production in pure iron was calculated using the full cascades damage energy method as shown in Fig. 2. Since 94% of ^{10}B $(n, \alpha)^{7}$Li reactions emit 0.84 MeV Li and 1.47 MeV He ions, the radiation damage was mostly induced by 0.84 MeV Li ions below 1.5 μm penetration radius, and 1.47 MeV He ions (Fig. 2(a)) in the region from 1.5 μm to 2.5 μm, where the peak radiation damage was below 40% of that of Li ions. The radiation damage in tungsten (Fig. 3) was lower than that of iron due to higher displacement energy ($E_{d} = 40$ eV for Fe and 90 eV for W) and lattice binding energy (5.8 eV for Fe and 13.2 eV for W).

Note that Figs. 2 and 3 are produced from SRIM simulation which assumes a 1D geometry where the "Depth" x is aligned with the initial ion (^{4}He or ^{7}Li) momentum, and the distribution of Frenkel pair, helium deposition, *etc.* are described by a 1D distribution $dP = \rho(x)dx$, $x = [0,\infty)$ shown in these figures. As illustrated in Fig. 1, however, since the initial ion momenta are spherically random within 4π solid angle, the actual distribution of vacancy concentration *etc.* will be a spherical distribution, $dP = \rho_{\text{radial}}(r)$ $4\pi r^{2}dr$, $r = [0,\infty)$. Even though numerically $r = x$, the radial fan-out would induce a transformation:

$$
\rho(x)\text{d}x = \rho(r)\text{d}r = \rho_{\text{radial}}(r)4\pi r^{2}\text{d}r \tag{3}
$$

so we obtain

$$
\rho_{\text{radial}}(r) = \rho(r) \big/ 4\pi r^{2} \tag{4}
$$

and therefore if there is a single emission source embedded in the 3D matrix like a stationary boride particle, the $\rho_{\text{radial}}(r)$ distribution can have two peaks, one at $r = 0$ where $\rho_{\text{radial}}(r{\rightarrow}0)$ turns singular

Fig. 4 shows the peak damage region of Li (~1 μm) and He (~2 μm) in iron and tungsten emitted from ^{10}B isotopes with slightly different peak locations. At initial irradiation time, or low burnup, the radiation damage structure surrounding ^{10}B rich precipitates could be characteristically distinguished as a double-ring damaged structure. This hypothetical concentric region, however, should not be observed in reality after heavy neutron irradiation, because the radiation damage and helium ions will be homogenously distributed in the case of the solid solution of ^{10}B in iron and tungsten. Even if some of ^{10}B segregate on grain boundaries, if the average grain size is smaller than 1 μm, helium concentration and radiation damage will be uniformly distributed inside the grains due to ballistic atomic mixing and radiation-enhanced diffusivity, as shown in Fig. 5. Furthermore, even with a concentrated ^{10}B source like a boride particle at the center initially, this boride particle is unlikely to stay fixed at the center, but is likely to fragment into "bomblets", splintering off and scattered around inside the material after a number of ^{10}B$(n, \alpha)^{7}$Li reactions, due to the extreme energetic nature of the product nuclei and the Coulomb explosion of the electron cloud left behind. Thus later on, the distribution of the dpa and appm (He) could automatically become much more homogenized due to the "nano-bomblets" effect.

3.2. Boron solubility and segregation

The equilibrium solubility of boron in tungsten is approximately 2,000 appm at 2,500 °C [29,30], which is enough amount to induce fusion-level helium generation using ^{10}B-enriched isotopes. However, the solid solubility of boron in iron at thermodynamic equilibrium is relatively low as 81 wt parts per million (wppm) in α-iron
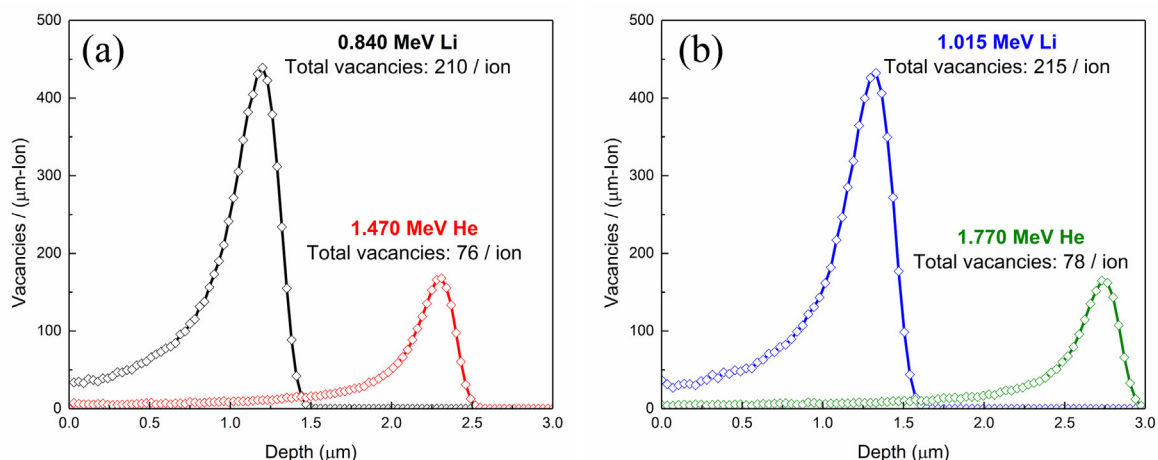

Fig. 2. SRIM-calculated vacancies production induced in iron (a) by 94% of ^{10}B$(n, \alpha)^{7}$Li reactions (b) by 6% of ^{10}B$(n, \alpha)^{7}$Li reactions.
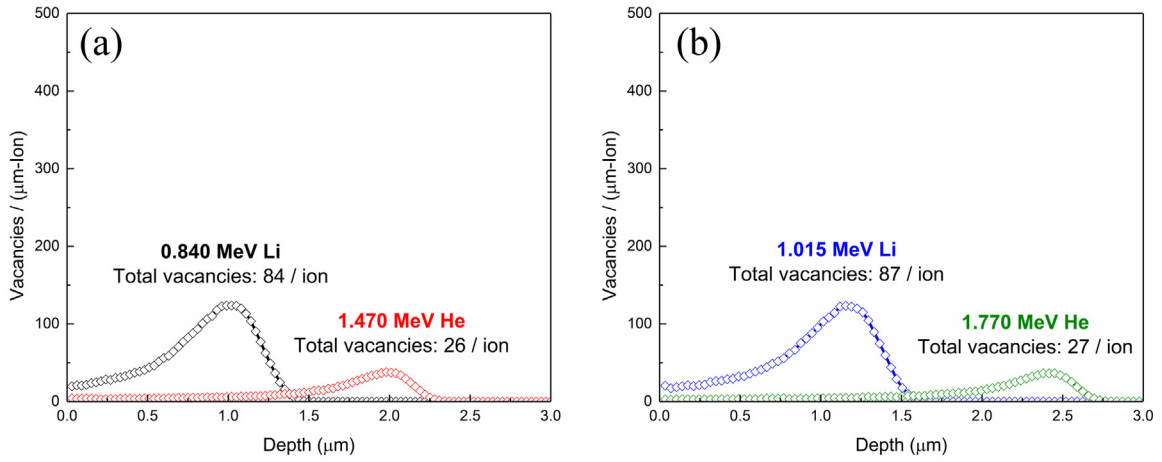
Fig. 3. SRIM-calculated vacancies production induced in tungsten (a) by 94% of ^{10}B$(n, \alpha)^7$Li reactions (b) by 6% of ^{10}B$(n, \alpha)^7$Li reactions.
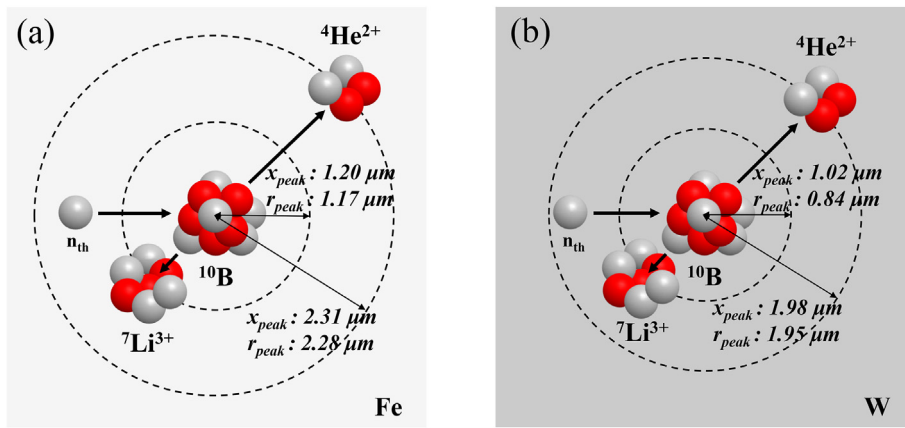
Fig. 4. Peak damage region of 1D (x_{peak}) and 3D (r_{peak}) geometry induced by ^{10}B $(n, \alpha)^7$Li reactions in (a) iron (b) tungsten.
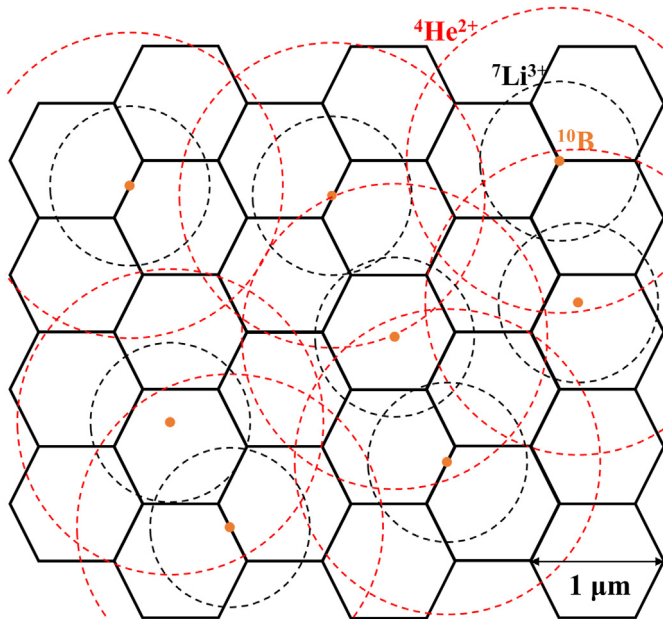
Fig. 5. Ion distribution of He and Li ions emitted from ^{10}B particles in iron with an average grain size of 1 μm.
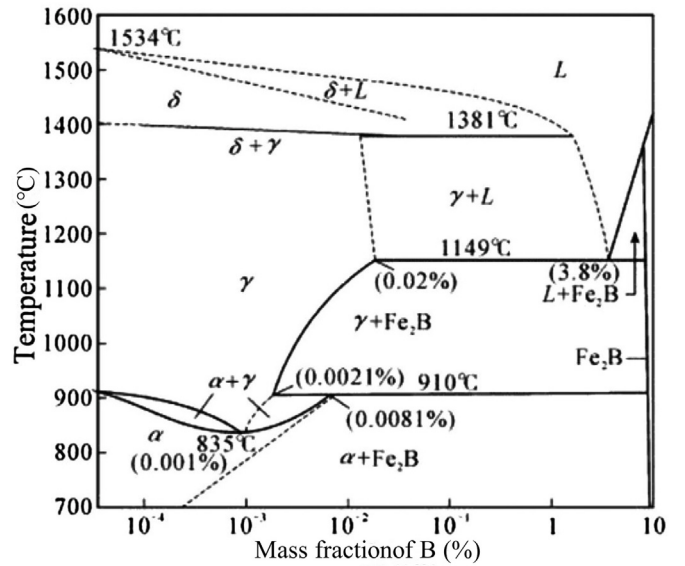
Fig. 6. Phase diagram of Fe-B [32] (taken with permission from the publisher).

at 910 °C and 200 wppm in γ-iron at 1 149 °C, corresponding to 418 appm and 1,032 appm, respectively (Fig. 6) [30]. The relatively low boron solubility in iron is considered due to its atomic diameter of 1.8 Å, which is not only too small for the substitutional position in iron (2.52 Å) but also too large for the interstitial site (octahedral interstitial site in α-iron = 0.38 Å and octahedral interstitial site in γ-iron = 1.085 Å) [31].

There are several ways for enhancing boron solubility in Fe-based alloys. Using metallic alloying elements such as chromium, vanadium, and molybdenum can expand the iron lattice to allow boron atoms to occupy the interstitial sites [33]. Since reduced activation ferritic/martensitic (RAFM) steels, one of the candidate structural materials for fusion reactors, have 8%−9%(in mass) Cr and 0.15%−0.25%(in mass) V, the boron solubility of RAFM will be expected to be higher than that in pure iron. Out-of-equilibrium effects in irradiated materials such as radiation-induced mixing, vacancy production, and vacancy-induced precipitate dissolution could also enhance the "dynamic" boron solubility and allow homogenous helium and radiation damage generation during neutron irradiation [34,35].

3.3. Neutron irradiation at HFIR

Since ^{10}B has an extremely high neutron capture cross-section of 3840 b for thermal neutron, neutron irradiation in a thermal reactor such as the HFIR and Petten High Flux Reactor will result in complete transmutation of ^{10}B within ~1 dpa [17,36]. The vacancy productions per each ion (Li and He) were calculated in iron and tungsten, considering the reaction probability as shown in Table 1. For example, each Li and He ion would knock out 210 and 76 iron atoms from their original lattice site, respectively. A single ^{10}B$(n, \alpha)^7$Li reaction in the iron, therefore, would produce 286 displacements and one helium gas atom, corresponding to 3,491 He appm/dpa. This could be used to control the ratio of helium production to radiation damage (appm/dpa) in neutron irradiation by changing the ^{10}B concentration.

The neutron irradiations of Fe and W doped with various ^{10}B concentrations at HFIR were computationally designed to mimic fusion conditions as shown in Table 2. The calculation was conducted based on one-cycle neutron irradiation (25 days) with a fast neutron flux of 1.2×10^{15} (n/(cm^2·s)) and a thermal neutron flux of 2.4×10^{15} (n/(cm^2·s)) [37]. The radiation damage induced by fast neutron (>0.1 MeV) was calculated based on the previous studies [38,39]. The radiation damage induced by ^{10}B$(n, \alpha)^7$Li reactions was almost negligible at the low ^{10}B concentrations well matched to previous studies. However, considerable radiation damage was produced with increasing ^{10}B concentration (~13% of total radiation damage was induced by ^{10}B$(n, \alpha)^7$Li reactions in case of 1,000 appm ^{10}B doped Fe), which becomes even greater with increasing ^{10}B loading. These results showed that the radiation damage induced by He and Li ions should be considered to reduce errors in the dpa estimation.

Simulations of ^{10}B-doped iron showed the possibility of massive helium production, but additional radiation source is necessary to expedite radiation damage to hundreds of dpa, appropriate for

Table 1
Radiation damage induced by ^{10}B$(n, \alpha)^7$Li reactions on Fe and W considering reaction probability.

	Fe	W
Vacancies per Li ion	210	84
Vacancies per He ion	76	26
Total displacements	286	110
He appm/dpa	3,491	9,072

fusion conditions. To maximize the radiation damage during neutron irradiation with ppm-level concentration, ^{235}U co-dopants could be added to ^{10}B doped iron. The radiation damage induced by fission reaction was estimated using SRIM simulations with following assumptions. The vacancies induced by gamma ray, fission neutron, and beta particles from ^{235}U fission were ignored, considering low energy (<10 MeV) compared to fission fragments (~168 MeV). The fission fragments were assumed to be ^{95}Kr and ^{137}Ba, the most probable fragment masses. The fissions per initial fissile atoms (FIFA) was estimated to be 14.5% during one-cycle neutron irradiation in HFIR considering the fission cross section of ^{235}U (ENDF/B-VIII.0). The SRIM simulation on ^{235}U-codoped iron showed that each ^{95}Kr and ^{137}Ba ion would knock out 24,374 and 45,243 iron atoms, respectively. For example, the radiation damage of iron doped with 1,000 appm ^{235}U could achieve ~10 dpa after the one-cycle neutron irradiation in HFIR. The radiation damage (~100 dpa) and helium production (~1,000 appm) for Fe-based fusion structural materials could be achieved by the neutron irradiation of iron doped with 1,000 appm ^{10}B and 9,700 appm ^{235}U as shown in Table 2. The irradiation tests for W-based fusion materials were also computationally designed to mimic the fusion conditions (~26 dpa, ~13 He appm) [40].

Fig. 7(a) shows the total radiation damage and helium generation of neutron-irradiated iron at HFIR with various ^{10}B concentrations after the one-cycle irradiation. It should be noted that ^{10}B does not produce radiation damage and He continually during the neutron irradiation. The half-life of burnt ^{10}B was estimated to be 0.9 days, which suggests that most helium and radiation damage generation will occur at the very beginning of neutron irradiation. This initial concentrated generation could be mitigated by using a thermal neutron shielding such as a Eu$_2$O$_3$-shield capsule that can slow down the transmutation closer to a fusion reactor condition as maintaining the amount of radiation damage and helium generation after the neutron irradiation [35]. The boron-10 doping combined with ^{235}U co-doping can shorten the radiation campaign to less than 2 months as shown in Fig. 8(a), while still reaching thousands of appm (He) and hundreds of dpa. Therefore, our proposed methodology can greatly reduce the time and cost of neutron irradiation tests for fusion reactor materials, which can greatly accelerate fusion structural materials selection and optimization.

3.4. Neutron irradiation at MITR

The fast neutron ($E > 0.1$ MeV) flux and thermal neutron flux of MITR are 1.3×10^{14} n/(cm^{2}s) and 3.4×10^{13} n/(cm^2·s), respectively. The thermal neutron fluence of MITR (1.3×10^{20} n/cm^2) is much lower than that of HFIR (5.2×10^{21} n/cm^2), which would not transmute all ^{10}B after the one-cycle irradiation (45 days). The burn-up of ^{10}B isotope under neutron irradiation (F) was estimated to be ~0.4 using Eqn. (3) [41].

$$F = 1 - \exp(-\sigma_\alpha \varphi_{\text{th}} t) \qquad (3)$$

where σ_α is the thermal neutron capture cross-section of ^{10}B, φ_{th} is the thermal neutron flux at MITR, and t is the irradiation time.

The radiation damage induced by both neutron and ^{10}B$(n, \alpha)^7$Li reactions for one cycle in MITR is relatively low than HFIR, which suggests higher ^{235}U and ^{10}B dopant concentrations is required as shown in Table 3. The ^{10}B and ^{235}U doping methodology can greatly enhance the irradiation capability of MITR by 500 times (from 0.008 dpa/day to ~4 dpa/day) with hundreds appm of helium production, as shown in Fig. 8(b), which allows rapid investigation of helium effect on fusion structural materials.

Table 2
Helium generation and radiation damage of ^{10}B-doped Fe and W irradiated at HFIR for 25 days.

| Material	Dopant concentration (appm)		He generation (appm)	Radiation damage (dpa)			He appm/dpa
	^{10}B	^{235}U		Neutron (>0.1 MeV)	^{10}B$(n, \alpha)^7$Li	Fission reaction	
Fe	1,000	0	1,000	1.9	0.300	0	455.0
	1,000	1,000				10.0	82.0
	1,000	9,600				98.0	10.0
W	13	0	13	0.8	0.001	0	16.0
	13	13				0.1	14.0
	13	4,000				25.0	0.5
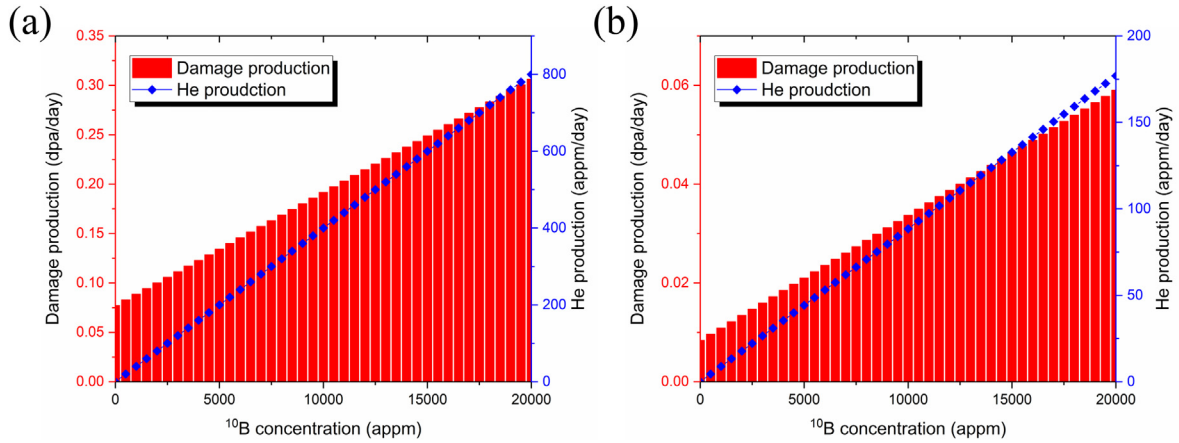
Fig. 7. Radiation damage production and helium production of iron doped with various ^{10}B (a) neutron irradiation at HFIR (the half-life of burnt ^{10}B was ~0.9 days) (b) neutron irradiation at MITR (the half-life of burnt ^{10}B was ~61.4 days).
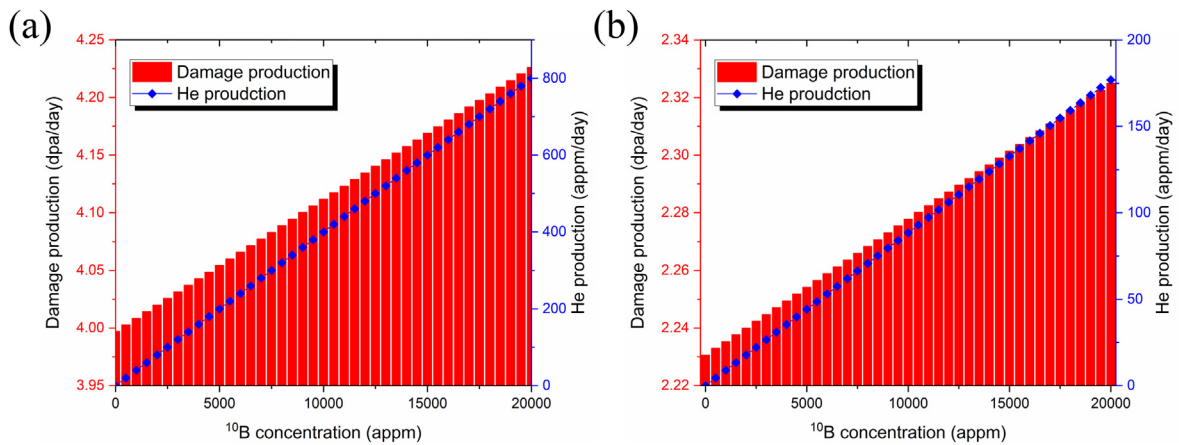

Fig. 8. Radiation damage production and helium production of iron doped with ^{10}B and ^{235}U (a) neutron irradiation with 9700 appm ^{235}U at HFIR (b) neutron irradiation with 26,000 appm ^{235}U at MITR.

Table 3
Helium generation and radiation damage of ^{10}B-doped Fe and W irradiated at MITR for 45 days.

| Material	Dopant concentration (appm)		He generation (appm)	Radiation damage (dpa)			He appm/dpa
	^{10}B	^{235}U		Neutron (>0.1 MeV)	^{10}B$(n, \alpha)^7$Li	Fission reaction	
Fe	2,600	0	995	0.4	0.300	0	1421.0
	2,600	2,600				10.0	93.0
	2,600	26,000				100.0	10.0
W	32	0	13	0.2	0.001	0	65.0
	32	32				0.1	43.0
	32	11,000				26.0	0.5
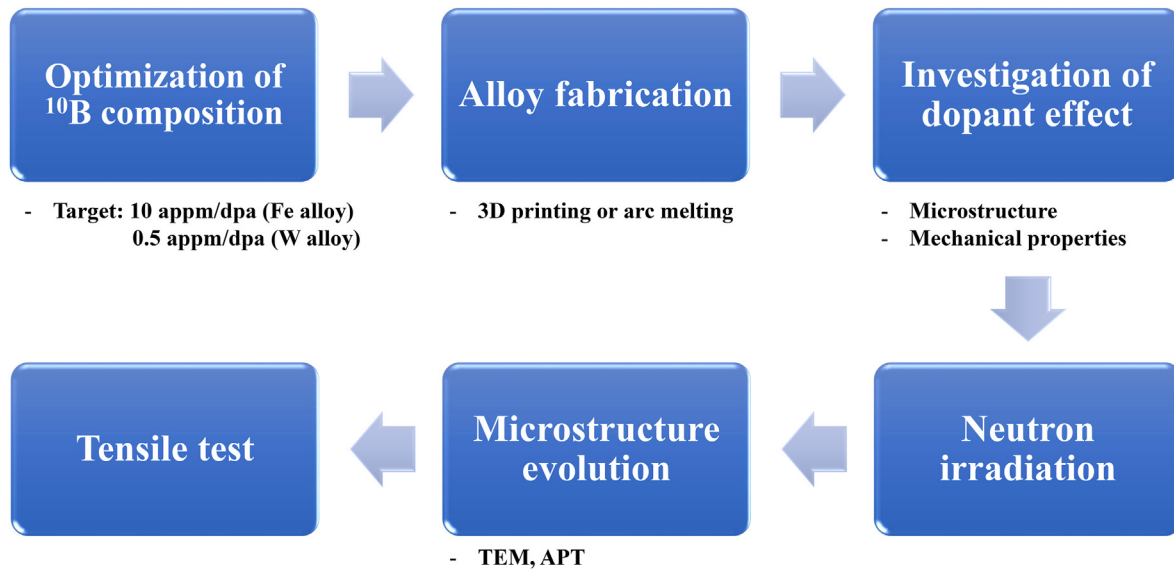
Fig. 9. Flowchart of ^{10}B doping methodology.

3.5. Design of doping methodology

Fig. 9 shows the envisioned flow chart of the boron doping technique to investigate the effects of helium concentration on material properties. First, the ^{10}B concentration will be determined based on the ratio of helium production ratio to radiation damage. Since the radiation damage induced by neutron and ^{10}B(n, α)^{7}Li reactions in the research reactor is not enough to emulate the fusion environment, additional sources for radiation damage such as ^{235}U will be necessary to achieve the target radiation damage.

The fabrication of uniformly dispersed ^{10}B in iron and tungsten is the key step to simulating the homogenous helium production and radiation damage since discrete halos were often observed around ^{10}B rich precipitates after neutron irradiation [17]. Arc melting could be utilized, which showed no B precipitates observed even though the B concentration exceeds the solubility limit in the iron (500 appm at the 1,050 °C annealing temperature) [11]. Other methods such as 3D printing can also be considered. The microstructure of fabricated alloys will be observed to confirm the presence of boron precipitates. Mechanical properties will be measured not only to investigate the dopant effect but also to compare the properties before and after the neutron irradiation.

420 stainless steel (420 SS) powders were provided from Höganäs. The particle size ranges from 20 to 63 μm. ^{10}B powders with average particle diameter 200 μm were purchased from American Elements. Large ^{10}B particles were ball-milled in a Fritsch Pulverisette 7 using 5 mm diameter of stainless steel balls and vials (ball to powder ratio of 5) for 15 h in order to reduce their particle size before blending them with 420 SS powders. Afterwards, ^{10}B powders were mixed with 420 SS powders to form a mixture of 2 600 appm ^{10}B and blended in batches of 500 g in a high-speed blender (VM0104, Vita-Mix, USA) for 90 min ^{10}B doped 420 SS composite powders were printed *via* laser powder bed fusion (LPBF) using a commercial system (EOS M290) as shown in Fig. 10. The parameter set was determined based on data from previously published LPBF study of AISI 420 [42].

^{10}B-doped samples and ^{11}B-doped samples will be irradiated at thermal research reactors to separate the effect of chemistry modification from irradiation effects. Since the thermal neutron flux of HFIR is high enough to transmute all ^{10}B at the very beginning of neutron irradiation, thermal neutron shielding capsules for

samples could be utilized to slow down the transmutation, closer to the fusion reactor environment [34].

The microstructure of the irradiated sample will be characterized using transmission electron microscopy (TEM) and atom probe tomography (APT) to confirm the homogeneous helium bubble formation. The size and density of helium bubbles will be measured after the irradiation [43]. Tensile tests will be also conducted to investigate the effect of helium on strength or ductility. By this approach, we should be able to shorten the radiation campaigns to achieve rapid helium generation and expedite fusion materials testing from many years down to months or even days.

4. Conclusion

The isotopically pure ^{10}B doping methodology on iron and tungsten was proposed to simulate the extreme environments inside fusion reactors with a high He appm-to-dpa ratio. Computational modeling of the radiation damage showed that a single ^{10}B(n, α)^{7}Li reaction can produce 286 displacements in iron and 110 displacements in tungsten corresponding to 3,491 He appm/dpa and 9,072 He appm/dpa, respectively. Considerable radiation displacement was induced by ^{10}B(n, α)^{7}Li reactions (>10% total radiation displacements in 1.000 appm ^{10}B doped Fe samples), which becomes even greater with increasing ^{10}B concentration. Therefore, the radiation damage induced by Li and He ions should be considered to minimize the errors in the dpa estimation.

The boron segregation to grain boundaries, the main problem of previous boron doping, could be overcome by more homogenous distribution of ^{10}B. Spatially homogenous radiation damage and helium generation were expected for grain sizes less than 1 μm, even if the boron partially formed precipitates or segregates on grain boundaries. Several factors such as metallic alloying, radiation-induced mixing, and vacancy-induced precipitate dissolution could also suppress boron segregation in iron and tungsten.

Feasibility studies on neutron irradiation with various ^{10}B concentrations in fission research reactor were performed to estimate helium generation and radiation damage. One-cycle neutron irradiation at HFIR showed that a complete burn-up of ^{10}B could be achieved, although the burn-up after the one-cycle at MITR was estimated to be ~40%. The simulation results showed that the ^{10}B and ^{235}U doping methodology in both HFIR and MITR can simulate
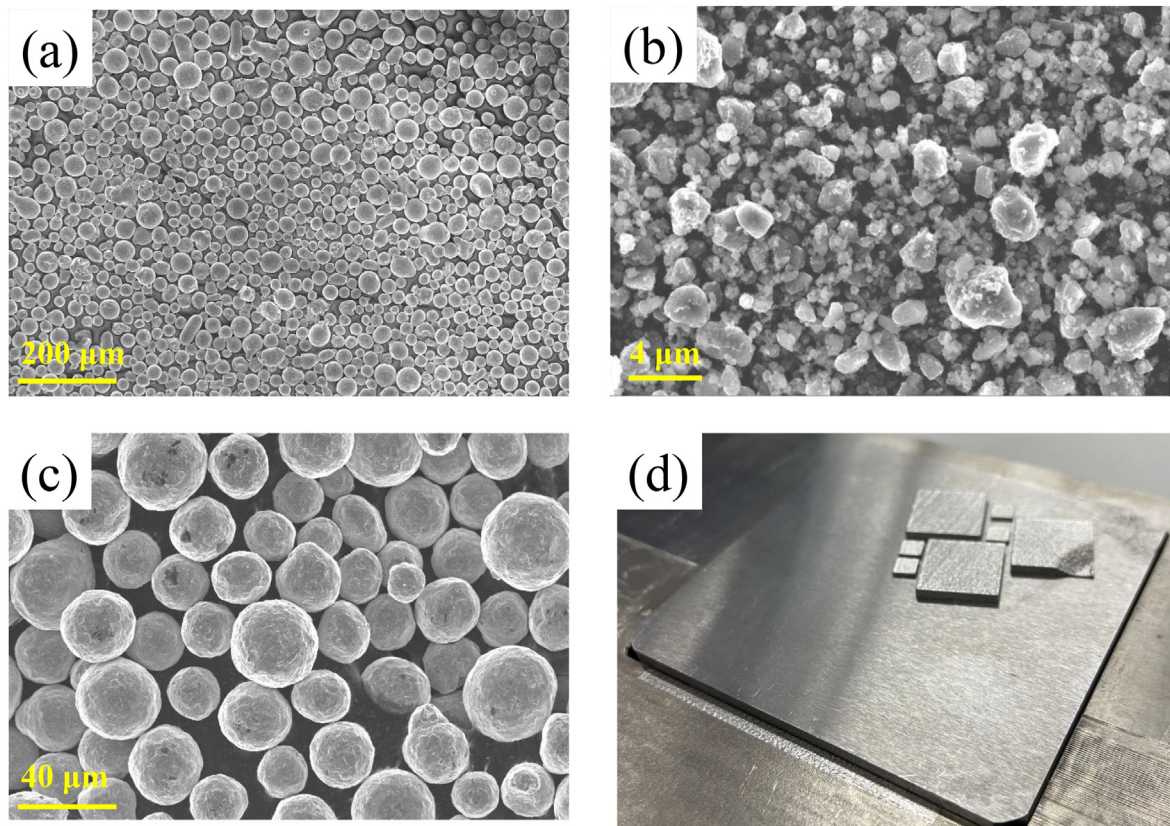
**Fig. 10.** (a) 420 SS powders for 3D printing, (b) Ball-milled [10]B particles, (c) [10]B doped 420 SS composite powders, and (d) 3D printed [10]B doped SS samples via lase powder bed fusion.

the extreme environment of fusion structural materials with high displacement rate (~4 dpa/day) and helium production rate (hundreds of appm/day). This proposed method would closely mimic fusion conditions and can greatly expedite fusion materials testing from many years down to months or even days, which can accelerate the design and qualification of fusion structural materials.

Declaration of competing interest

The authors declare that they have no known competing financial interests or personal relationships that could have appeared to influence the work reported in this paper.

Acknowledgments

References

[1] Kuang AQ, Cao NM, Creely AJ, Dennett CA, Hecla J, LaBombard B, et al. Conceptual design study for heat exhaust management in the ARC fusion pilot plant. Fusion Eng Des 2018;137:221−42. https://doi.org/10.1016/j.fusengdes.2018.09.007.

[2] Mansur LK, Grossbeck ML. Mechanical property changes induced in structural alloys by neutron irradiations with different helium to displacement ratios. J Nucl Mater 1988;155−157:130−7. https://doi.org/10.1016/0022-3115(88)90235-8.

[3] Schroeder H, Ullmaier H. Helium and hydrogen effects on the embrittlement of iron-and nickel-based alloys. J Nucl Mater 1991;179−181:118−24. https://doi.org/10.1016/0022-3115(91)90025-3.

[4] Gilbert MR, Dudarev SL, Zheng S, Packer LW, Sublet JC. An integrated model for materials in a fusion power plant: transmutation, gas production, and helium embrittlement under neutron irradiation. Nucl Fusion 2012;52. https://doi.org/10.1088/0029-5515/52/8/083019.

[5] Molvik A, Ivanov A, Kulcinski GL, Ryutov D, Santarius J, Simonen T, et al. A gas dynamic trap neutron source for fusion material and subcomponent testing. Fusion Sci Technol 2010;57:369−94. https://doi.org/10.13182/FST10.

[6] Sawan ME. Damage parameters of structural materials in fusion environment compared to fission reactor irradiation. Fusion Eng Des 2012;87:551−5. https://doi.org/10.1016/j.fusengdes.2012.01.022.

[7] Xu HW, Kim SY, Chen D, Monchoux J-P, Voisin T, Sun C, et al. Materials genomics search for possible helium-absorbing nano-phases in fusion structural materials. Adv Sci 2022;9:2203555. https://doi.org/10.1002/advs.202203555.

[8] Huang J, Liu H, Gao Z, Su Y, Liu Q, Ge W, et al. Helium-Hydrogen synergistic effects in structural materials under fusion neutron irradiation. Front Mater 2022;9. https://doi.org/10.3389/fmats.2022.849115.

[9] Bhattacharya A, Meslin E, Henry J, Leprêtre F, Décamps B, Barbu A. Combined effect of injected interstitials and He implantation, and cavities inside dislocation loops in high purity Fe-Cr alloys. J Nucl Mater 2019;519:30−44. https://doi.org/10.1016/j.jnucmat.2019.03.043.

[10] Zinkle SJ, Möslang A. Evaluation of irradiation facility options for fusion materials research and development. Fusion Eng Des 2013;88:472−82. https://doi.org/10.1016/j.fusengdes.2013.02.081.

[11] Lisowski PW, Bowman CD, Russell GJ, Wender SA. Los alamos national laboratory spallation neutron sources. Nucl Sci Eng 1990;106:208−18. https://doi.org/10.13182/NSE90-A27471.

[12] Schneider H-C, Dafferner B, Aktaa J. Embrittlement behaviour of different international low activation alloys after neutron irradiation. J Nucl Mater 2001;295:16−20. https://doi.org/10.1016/S0022-3115(01)00508-6.

[13] Shiba K, Hishinuma A. Low-temperature irradiation effects on tensile and Charpy properties of low-activation ferritic steels. J Nucl Mater 2000;283−287:474−7. https://doi.org/10.1016/S0022-3115(00)00369-X.

[14] Rieth M, Dafferner B, Röhrig HD. Embrittlement behaviour of different international low activation alloys after neutron irradiation. J Nucl Mater 1998;258−263:1147−52. https://doi.org/10.1016/S0022-3115(98)00171-8.

[15] Okita T, Wolfer WG, Garner FA, Sekimura N. Influence of boron on void swelling in model austenitic steels. J Nucl Mater 2004;329−333:1013−6. https://doi.org/10.1016/j.jnucmat.2004.04.126.

[16] Wakai E, Hashimoto N, Miwa Y, Robertson JP, Klueh RL, Shiba K, et al. Effect of helium production on swelling of F82H irradiated in HFIR. J Nucl Mater 2000;283–287:799–805. https://doi.org/10.1016/S0022-3115(00)00268-3.

[17] Miwa Y, Wakai E, Shiba K, Hashimoto N, Robertson JP, Rowcliffe AF, et al. Swelling of F82H irradiated at 673 K up to 51 dpa in HFIR. J Nucl Mater 2000;283–287:334–48. https://doi.org/10.1016/S0022-3115(00)00222-1.

[18] Klimenkov M, Möslang A, Materna-Morris E, Schneider H-C. Helium bubble morphology of boron alloyed EUROFER97 after neutron irradiation. J Nucl Mater 2013;442:S52. https://doi.org/10.1016/j.jnucmat.2013.04.022. S57.

[19] Best SE, Fadaai A, Harling OK. Initial results using splat cooling in the development of boron doping for the simulation of fusion reactor helium embrittlement. J Nucl Mater 1979;85–86:835–8. https://doi.org/10.1016/0022-3115(79)90363-5.

[20] Vitek JM, Klueh RL. Microstructure of 9 Cr-1 MoVNb steel irradiated to 36 dpa at elevated temperatures in HFIR. J Nucl Mater 1984;122:254–9. https://doi.org/10.1016/0022-3115(84)90606-8.

[21] Maziasz PJ, Klueh RL, Vitek JM. Helium effects on void formation in 9Cr-1MoVNb and 12Cr-1MoVW irradiated in HFIR. Nucl Mater 1986;141–143: 929–37. https://doi.org/10.1016/0022-3115(86)90120-0.

[22] Klueh RL, Maziasz PJ, Vitek JM. Postirradiation tensile behavior of nickel-doped ferritic steels. J Nucl Mater 1984;141–143:960–5. https://doi.org/10.1016/0022-3115(86)90125-X.

[23] Gelles DS, Garner FA. An experimental method to determine the role of helium in neutron-induced microstructural evolution. J Nucl Mater 1979;85–86: 689–93. https://doi.org/10.1016/0022-3115(79)90340-4.

[24] Materna-Morris E, Klimenkov M, Möslang A. The influence of boron on structural properties of martensitic 8-10%Cr-steels. Mater Sci Forum 2012;730–732:877–982. https://doi.org/10.4028/www.scientific.net/MSF.730-732.877.

[25] Shiba K, Suzuki M, Hishinuma A, Pawel JE. Effect of boron on post irradiation tensile properties of reduced activation ferritic steel (F-82H) irradiated in HFIR. Washington (DC): U.S. Department of Energy; 1994 Dec. Report No.: CONF-940657-11. Contract No.: AC05-84OR21400.

[26] Ziegler JF, Ziegler MD, Biersack JP. SRIM - the stopping and range of ions in matter. Nucl Instrum Methods Phys Res B 2010;268:1818–23. https://doi.org/10.1016/j.nimb.2010.02.091. 2010.

[27] Stoller RE, Toloczko MB, Was GS, Certain AG, Dwaraknath S, Garner FA. On the use of SRIM for computing radiation damage exposure. Nucl Instrum Methods Phys Res B 2013;310:75–80. https://doi.org/10.1016/j.nimb.2013.05.008.

[28] Agarwal S, Lin Y, Li C, Stoller RE, Zinkle SJ. On the use of SRIM for calculating vacancy production: quick calculation and full-cascade options. Nucl Instrum Methods Phys Res B 2021;503:11–29. https://doi.org/10.1016/j.nimb.2021.06.018.

[29] Ren C, Yang Y, Li Y, Zhu Z, Li J. Sample spinning to mitigate polarization artifact and interstitial-vacancy imbalance in ion-beam irradiation. npj Comput Mater 2020;6:189. https://doi.org/10.1038/s41524-020-00438-9.

[30] Duschanek H, Rogl P. Critical assessment and thermodynamic calculation of the binary system boron-tungsten (B-W). J Phase Equilibria Diffus 1995;16: 150–61. https://doi.org/10.1007/BF02664852.

[31] Goldschmidt H, Catherall E, Ham W, Oliver D. Investigation into the tungsten-rich regions of the binary systems tungsten- carbon, tungsten-boron and tungsten-beryllium. 1963. United States. Report No: ASD-TDR-62-25(Pt.II).

[32] Zhang J, Liu J, Liao H, Zeng M, Ma S. A review on relationship between morphology of boride of Fe-B alloys and the wear/corrosion resistant properties and mechanisms. J Mater Res Technol 2019;8:6308–20. https://doi.org/10.1016/j.jmrt.2019.09.004.

[33] Zhang L, Demkowicz MJ. Radiation-induced mixing between metals of low solid solubility. Acta Mater 2014;76:135–50. https://doi.org/10.1016/j.actamat.2014.05.013.

[34] Schuler T, Nastar M, Soisson F. Vacancy-induced dissolution of precipitates in out-of-equilibrium systems: a test case of FeX (X= C,N,O) alloys. Phys Rev B 2017;95. https://doi.org/10.1103/PhysRevB.95.014113.

[35] Hashimoto N, Klueh RL, Shiba K. Pros and cons of nickel-and boron-doping to study helium effects in ferritic/martensitic steels. J Nucl Mater 2002;307–311: 222–8. https://doi.org/10.1016/S0022-3115(02)01183-2.

[36] Ilas G, Chandler D, Ade B, Sunny E, Betzler B, Pinkston D. Modeling and simulations for the high flux isotope reactor cycle 400. Oak ridge (TN): Oak Ridge National laboratory, reactor and nuclear system division, research reactors division. 2015 Mar. Report No.: ORNL/TM-2015/36. Contract No.: DE-AC05-00OR22725. Sponsored by the Department of Energy.

[37] Horton LL, Bentley J, Farrell K. A TEM study of neutron-irradiated iron. J Nucl Mater 1982;108–109:222–3. https://doi.org/10.1016/0022-3115(82)90490-1.

[38] Hu X, Koyanagi T, Fukuda M, Kiran Kumar NAP, Snead LL, Wirth BD, et al. Irradiation hardening of pure tungsten exposed to neutron irradiation. J Nucl Mater 2016;480:235–43. https://doi.org/10.1016/j.jnucmat.2016.08.024.

[39] Sawan ME. Damage parameters of structural materials in fusion environment compared to fission reactor irradiation. Fusion Eng Des 2012;87:551–5. https://doi.org/10.1016/j.fusengdes.2012.01.022.

[40] Sawan ME. Damage parameters of structural materials in fusion environment compared to fission reactor irradiation. Fusion Eng Des 2012;87:551–5. https://doi.org/10.1016/j.fusengdes.2012.01.022.

[41] Mansur LK, Farrell K. On mechanisms by which a soft neutron spectrum may induce accelerated embrittlement. J Nucl Mater 1990;170:236–45. https://doi.org/10.1016/0022-3115(90)90294-W.

[42] Tian Y, Chadha K, Arans C. Laser powder bed fusion of ultra-high-strength 420 stainless steel: microstructure characterization, texture evolution and mechanical properties. Mater Sci Eng 2021;805:140790. https://doi.org/10.1016/j.msea.2021.140790.

[43] Gao R, Jin M-M, Li Q-J, So KP, Zhang L-F, Wang X-P, Fang Q-F, Sun C, Shao L, Li J. "Hybrid diffusive-displacive helium outgassing in Cu/Nb multilayer composites,". Scripta Materialia 2021;194:113706.

Yunsong Jung currently works as a Postdoctoral Researcher at the Korea Institute of Fusion Energy. He received his Ph.D. degree in nuclear engineering from Ulsan National Institute of Science and Technology and continued his research as a postdoctoral fellow at MIT. His primary research interests are irradiation effects on nuclear and fusion materials.

Ju Li has held faculty positions at the Ohio State University, the University of Pennsylvania, and is presently a chaired professor at MIT. His group (http://Li.mit.edu) investigates the mechanical, electrochemical and transport behaviors of materials as well as novel means of energy storage and conversion. Ju was elected Fellow of the American Physical Society in 2014, a Fellow of the Materials Research Society in 2017 and a Fellow of AAAS in 2020. He is the chief organizer of MIT A + B Applied Energy Symposia that aim to develop solutions to global climate change challenges with "A-Action before 2040" and "B-Beyond 2040" technologies.